



## UvA-DARE (Digital Academic Repository)

### Ultrathin complex oxide nanomechanical resonators

Davidovikj, D.; Groenendijk, D.J.; Monteiro, A.M.R.V.L.; Dijkhoff, A.; Afanasiev, D.; Šiškins, M.; Lee, M.; Huang, Y.; van Heumen, E.; van der Zant, H.S.J.; Caviglia, A.D.; Steeneken, P.G.

**DOI**

[10.1038/s42005-020-00433-y](https://doi.org/10.1038/s42005-020-00433-y)

**Publication date**

2020

**Document Version**

Final published version

**Published in**

Communications Physics

**License**

CC BY

[Link to publication](#)

**Citation for published version (APA):**

Davidovikj, D., Groenendijk, D. J., Monteiro, A. M. R. V. L., Dijkhoff, A., Afanasiev, D., Šiškins, M., Lee, M., Huang, Y., van Heumen, E., van der Zant, H. S. J., Caviglia, A. D., & Steeneken, P. G. (2020). Ultrathin complex oxide nanomechanical resonators. *Communications Physics*, 3, Article 163. <https://doi.org/10.1038/s42005-020-00433-y>

**General rights**

It is not permitted to download or to forward/distribute the text or part of it without the consent of the author(s) and/or copyright holder(s), other than for strictly personal, individual use, unless the work is under an open content license (like Creative Commons).

**Disclaimer/Complaints regulations**

If you believe that digital publication of certain material infringes any of your rights or (privacy) interests, please let the Library know, stating your reasons. In case of a legitimate complaint, the Library will make the material inaccessible and/or remove it from the website. Please Ask the Library: <https://uba.uva.nl/en/contact>, or a letter to: Library of the University of Amsterdam, Secretariat, Singel 425, 1012 WP Amsterdam, The Netherlands. You will be contacted as soon as possible.

*UvA-DARE is a service provided by the library of the University of Amsterdam (<https://dare.uva.nl>)*

## Ultrathin complex oxide nanomechanical resonators

D. Davidovikj <sup>1,4</sup>, D. J. Groenendijk<sup>1,4</sup>, A. M. R. V. L. Monteiro<sup>1</sup>, A. Dijkhoff<sup>1</sup>, D. Afanasiev<sup>1</sup>, M. Šiškins <sup>1</sup>, M. Lee<sup>1</sup>, Y. Huang<sup>2</sup>, E. van Heumen <sup>2</sup>, H. S. J. van der Zant <sup>1</sup>, A. D. Caviglia<sup>1</sup>✉ & P. G. Steeneken <sup>1,3</sup>✉

Complex oxide thin films and heterostructures exhibit a variety of electronic phases, often controlled by the mechanical coupling between film and substrate. Recently it has become possible to isolate epitaxially grown single-crystalline layers of these materials, enabling the study of their properties in the absence of interface effects. In this work, we use this technique to create nanomechanical resonators made out of SrTiO<sub>3</sub> and SrRuO<sub>3</sub>. Using laser interferometry, we successfully actuate and measure the motion of the nanodrum resonators. By measuring the temperature-dependent mechanical response of the SrTiO<sub>3</sub> resonators, we observe signatures of a structural phase transition, which affects both the strain and mechanical dissipation in the resonators. Here, we demonstrate the feasibility of integrating ultrathin complex oxide membranes for realizing nanoelectromechanical systems on arbitrary substrates and present a novel method of detecting structural phase transitions in these exotic materials.

<sup>1</sup>Kavli Institute of Nanoscience, Delft University of Technology, P.O. Box 50462600 GA Delft, The Netherlands. <sup>2</sup>Van der Waals - Zeeman Institute, Institute of Physics (IoP), University of Amsterdam, Science Park 904, 1098 XH Amsterdam, The Netherlands. <sup>3</sup>Department of Precision and Microsystems Engineering, Delft University of Technology, Mekelweg 2, 2628 CD Delft, The Netherlands. <sup>4</sup>These authors contributed equally: D. Davidovikj, D. J. Groenendijk. ✉email: [a.caviglia@tudelft.nl](mailto:a.caviglia@tudelft.nl); [p.g.steeneken@tudelft.nl](mailto:p.g.steeneken@tudelft.nl)

It is well established that the electronic and magnetic properties of complex oxides are extremely sensitive to mechanical strain due to the strong coupling between the lattice and the charge, spin, and orbital degrees of freedom<sup>1–6</sup>. This sensitivity stems from rotations and distortions of the corner-connected BO<sub>6</sub> octahedra (where B is a transition metal ion situated in the centre of the octahedron formed by the oxygen atoms), which determine the overlap between orbitals on adjacent atomic sites<sup>7</sup>. The B–O bond lengths and rotation angles are routinely controlled by strain through heteroepitaxy, which forms a powerful tool to tune the properties of ultrathin films. The strong dependence of their electronic properties on mechanical strain has attracted a lot of attention towards their implementation in nanoelectromechanical sensors and actuators<sup>8</sup>, but exploiting this trait to the fullest has been limited by the requirement of a substrate for the epitaxial growth. This constrains the possibilities for their mechanical manipulation and integration with electronics and it could not be circumvented until recently, when single-crystal films of complex oxides were successfully released and transferred<sup>9,10</sup>. This sparked a new wave of interest in studying the properties of these materials, this time in their isolated, ultrathin form<sup>11</sup>.

On the other hand, a wide variety of mechanical manipulation techniques have been developed for van der Waals materials<sup>12</sup>, where weak interlayer bonding enables exfoliation of single- and few-layer films. Their ease of manipulation has enabled the top-down fabrication of nanomechanical elements, such as suspended membranes and ribbons. This, combined with their flexibility, low mass, and remarkable strength, has made them promising candidates for nanomechanical sensing applications<sup>13–16</sup>. Conversely, the well-developed field of nanomechanics has established a solid basis for characterizing the thermal and mechanical properties of van der Waals materials<sup>17–19</sup>.

In this work, we utilize the fabrication techniques for van der Waals materials to realize ultrathin nanomechanical resonators made out of epitaxially grown single-crystal complex oxide films. We show that these devices can be used to detect signatures of temperature-induced phase transitions of the material, which manifest themselves through changes of strain and, even more prominently, of mechanical dissipation in the resonators.

## Results

**Fabrication of complex oxide nanodrums.** The fabrication of the complex oxide mechanical resonators is described in Fig. 1. To isolate the epitaxial SrTiO<sub>3</sub> (STO) and SrRuO<sub>3</sub> (SRO) thin films from the substrate, a water-soluble epitaxial Sr<sub>3</sub>Al<sub>2</sub>O<sub>6</sub> (SAO) layer is first deposited by pulsed laser deposition on a TiO<sub>2</sub>-terminated STO(001) substrate (see ‘Methods’). Figure 1a shows the reflection high-energy electron diffraction (RHEED) intensity of the specular spot during the growth of SAO and STO. Oscillations are observed during the growth of both films, indicating that the growth occurs in layer-by-layer mode. Atomic force microscopy (AFM) topographic maps are shown in Fig. 1b, c, showing that the STO surface has a step-and-terrace structure, corroborating the growth mode. An X-ray diffraction (XRD) measurement of an SRO/SAO/STO heterostructure is shown in Supplementary Fig. 1 and discussed in Supplementary Note 1.

To dissolve the sacrificial layer and release the thin film from the substrate, a polydimethylsiloxane (PDMS) layer is attached to the surface before the entire stack is immersed in deionized water. After the dissolution of the SAO layer (approximately 1 h for a 5 × 5 mm<sup>2</sup> 50-nm-thick SAO film, see Supplementary Movie 1), the film can be transferred onto other substrates such as Si/SiO<sub>2</sub> using a deterministic dry transfer technique<sup>20</sup>. An XRD measurement of a 10 unit cell (u.c.) STO flake on a Si/SiO<sub>2</sub> substrate is shown in Fig. 1d. Laue oscillations are clearly visible, indicating that the films are of excellent

crystalline quality after the release and transfer process. Since the film is no longer epitaxial on the substrate, the rocking curve (Fig. 1e) is a measure of the morphology of the STO film lying on the SiO<sub>2</sub>. The small full width at half maximum (0.95°) indicates that the film lies very flat on the Si/SiO<sub>2</sub> substrate. To fabricate nanomechanical resonators, we transfer the STO and SRO films onto Si/SiO<sub>2</sub> substrates pre-patterned with circular cavities (schematically shown in Fig. 1f), demonstrating the feasibility of creating suspended complex oxide membranes. An optical image of 9 u.c. (thickness:  $h = 3.6$  nm) thick SRO drums (diameter:  $d = 13$  μm) is shown in Fig. 1g. It is remarkable that these materials, much like their van der Waals counterparts, have the flexibility and tensile strength required to be suspended with aspect ratios exceeding  $d/h > 3600$ .

**Mechanical characterization of the nanodrums.** We characterize the high-frequency dynamics of the complex oxide nanodrums using the optical actuation and detection set-up shown in Fig. 1h. The drums are mounted in the vacuum chamber (10<sup>−6</sup> mbar) of a closed-cycle cryostat with optical access. Their motion is read out using a red HeNe laser ( $\lambda = 632.8$  nm). The complex oxide membrane and the silicon underneath form a Fabry–Pérot cavity, where the motion of the membrane modulates the intensity of the reflected light, which is measured by a photodiode. The resonators are actuated optothermally using a blue laser ( $\lambda = 405$  nm) that is coupled into the optical path via a cold mirror<sup>21,22</sup>. Measurements are performed in a homodyne detection scheme using a vector network analyser (VNA), simultaneously sweeping the actuation and detection frequencies.

The mechanical resonances of several STO and SRO drums are shown in Fig. 2. Although STO is transparent in the visible range<sup>23</sup>, the motion of the drums can still be actuated and measured optically since the refractive index of the STO is different from that of vacuum and the absorption edge of strained STO can shift to higher wavelengths<sup>24</sup>. Figure 2a, b shows measurements of two STO drums and Fig. 2c, d of two SRO drums of different diameters. Measurements over a wider frequency range show that higher-order resonances of the drums can also be detected; two examples are shown in Fig. 2e, f, where up to four higher-order resonances are visible. By taking the ratio of the second harmonic ( $f_1$ ) to the fundamental mode ( $f_0$ ), we can estimate whether the mechanical properties are dictated by the pre-tension (theoretical ratio 1.59) or if they are dominantly determined by the bending rigidity (theoretical ratio 2.09), the latter being dependent on the Young’s modulus of the material ( $E$ ). It can be seen from Fig. 2c that the STO drums are in a crossover regime (ratio 1.72), similar to what has been observed in drums of similar dimensions made of MoS<sub>2</sub><sup>22</sup> and TaSe<sub>2</sub><sup>25</sup> (an AFM nanoindentation measurement of the sample characterized in Fig. 2c is shown in Supplementary Fig. 2 and the derivation of the extracted properties is outlined in Supplementary Note 2). On the other hand, the mechanical properties of the SRO drums are almost entirely determined by their pre-tension since  $f_1/f_0 = 1.47$ , which is close to the theoretical value of 1.59. Statistics on 18 STO drums are shown in Supplementary Fig. 3 and discussed in Supplementary Note 3.

**Temperature-dependent mechanical properties.** Having confirmed that the resonators can be mechanically characterized at room temperature, we now investigate how their mechanical properties change with temperature. The signal of the SRO drums <200 K was below the noise level of the measurement system, so systematic temperature-dependent measurements could only be performed on the STO drums. STO is known to undergo several phase transitions as a function of temperature. A phase transition is characterized by a discontinuity in specific heat<sup>26</sup>, which, depending

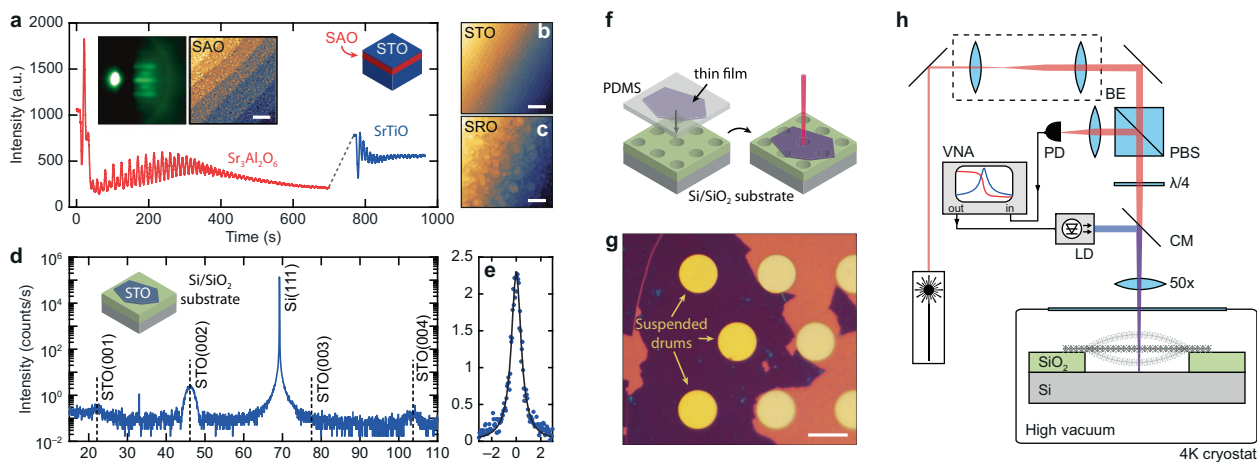


**Fig. 1 Sample fabrication and basic characterization.** **a** Reflection high-energy electron diffraction (RHEED) intensity oscillations during the growth of  $\text{Sr}_3\text{Al}_2\text{O}_6$  (SAO)—red line—and  $\text{SrTiO}_3$  (STO)—blue line. Inset: RHEED diffraction pattern and atomic force microscopic (AFM) image of the SAO surface. The scale bar is 200 nm. **b** AFM images of the STO and **c**  $\text{SrRuO}_3$  (SRO) film surfaces grown on top of the SAO. The scale bars are 1  $\mu\text{m}$ . **d** X-ray diffraction measurement of a 10 unit cell (u.c.) STO film transferred on a  $\text{Si}/\text{SiO}_2$  substrate. The expected peak positions are marked by the vertical dashed lines. **e** Rocking curve around the (002) reflection. **f** Schematics of the transfer of a thin SRO film onto a pre-patterned  $\text{Si}/\text{SiO}_2$  substrate. **g** Optical image of suspended 9 u.c. SRO drums with a diameter of 13  $\mu\text{m}$ . The purple surface is the area covered by the SRO film, including the three suspended drums marked by the arrows. The scale bar is 10  $\mu\text{m}$ . **h** Set-up for interferometric displacement detection (VNA vector network analyser, PD photodiode, LD laser diode, BE beam expander, PBS polarized beam splitter, CM cold mirror).

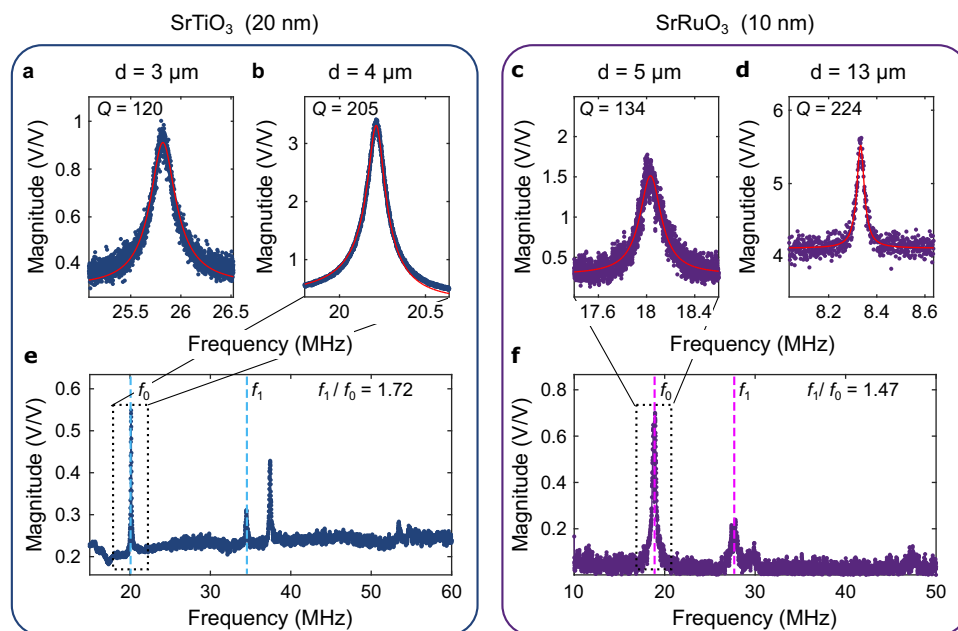


**Fig. 2 Mechanical characterization of  $\text{SrTiO}_3$  (STO) and  $\text{SrRuO}_3$  (SRO) nanodrums.** Resonance frequency measurements of 20-nm-thick STO and 10 nm-thick SRO nanodrums. **a, b** Frequency spectra of two STO drums with diameters of **a** 3  $\mu\text{m}$  and **b** 4  $\mu\text{m}$ . The red lines are linear harmonic oscillator fits. The extracted quality factors are shown in each of the panels. **c, d** Frequency spectra of two SRO drums with diameters of **c** 5  $\mu\text{m}$  and **d** 13  $\mu\text{m}$ . The red lines are linear harmonic oscillator fits. The extracted quality factors are shown in each of the panels. **e** A wide-range frequency spectrum of the drum shown in **b**. The positions of the fundamental resonance mode ( $f_0$ ) and the second resonance mode ( $f_1$ ) are marked with vertical dashed lines. **f** A wide-range frequency spectrum of the drum shown in **c**. The positions of the fundamental resonance mode ( $f_0$ ) and the second harmonic ( $f_1$ ) are marked with vertical dashed lines. The magnitude is a dimensionless number defined as the ratio of the input and output voltage of the vector network analyser.

on its magnitude, is expected to influence the mechanics of the membranes<sup>27</sup>, as it is closely related to the thermal expansion coefficient<sup>28</sup>. Figure 3 shows the mechanical properties of an STO nanodrum as a function of temperature. The temperature dependence of the resonance frequency (Fig. 3a) shows an evolution that is commonly observed in two-dimensional (2D) materials<sup>29–31</sup>. The

monotonic increase of  $f_0$  with decreasing temperature is usually ascribed to a difference in the thermal expansion coefficients between the membrane and the substrate<sup>30,31</sup>, which results in thermally induced tensile stress. The fact that the resonance frequency increases with decreasing temperature despite the decrease of the Young's modulus of bulk STO below the transition

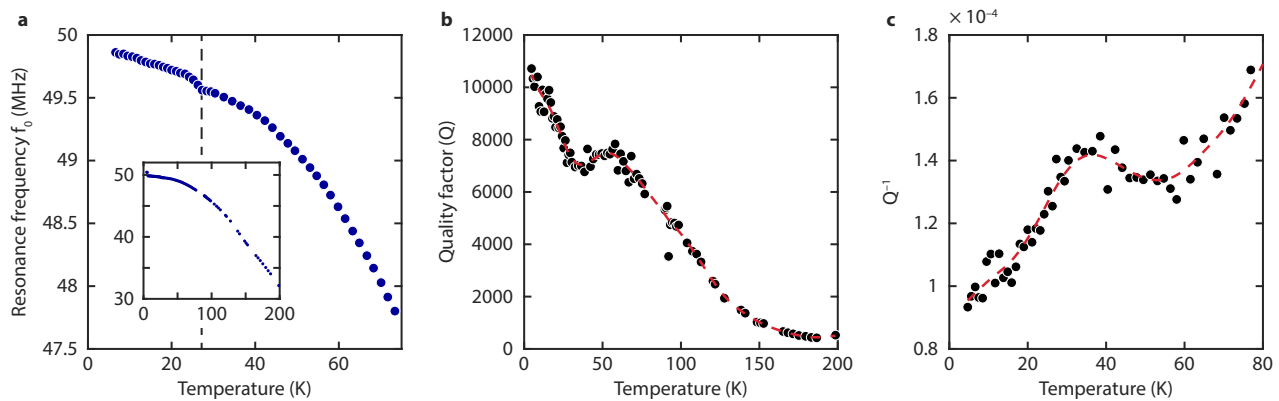


**Fig. 3** Temperature dependence of the mechanical properties of a 4- $\mu\text{m}$  SrTiO<sub>3</sub> (STO) drum. **a** Resonance frequency as a function of temperature (inset: temperature range 4–200 K). **b** Quality factor as a function of temperature. The red line is a guide to the eye (x-axis range goes to 200 K). **c** Inverse quality factor ( $Q^{-1}$ ) as a function of temperature in the region between 4 and 80 K. The fitting error for all graphs is within the size of the data points. For the  $Q$  factor, measurement-to-measurement fluctuations are observed with a standard deviation between 11% at 4 K and 4% at 200 K.

temperature<sup>32,33</sup> indicates that the mechanical behaviour of the resonator is dominated by tension, rather than bending rigidity<sup>22</sup>. Since the resonance frequency  $f_0$  is related to the effective thermal expansion coefficient of the system  $\alpha_{\text{eff}} (f_0^2 \propto \alpha_{\text{eff}}(T)\Delta T)$ , an abrupt change in  $\alpha_{\text{eff}}$  will noticeably affect  $f_0$ . Interestingly, a discontinuity is observed in  $f_0$  at around 30 K (Fig. 3a, dashed line), which coincides with the temperature at which the STO undergoes a structural phase transition, where the Sr ions disorder along [111] directions, rendering the structure locally triclinic<sup>34–36</sup>. This transition is accompanied by changes in mechanical properties<sup>32,33,37,38</sup>, as well as in the thermal expansion coefficient of STO<sup>39</sup>.

Another, more often discussed phase transition occurs in this material at 105 K, a temperature at which the cubic structure of bulk STO is known to break up into locally ordered tetragonal domains joined by ferroelastic domain walls<sup>40,41</sup>. Signatures of this transition are absent from the resonance frequency as a function of temperature (inset of Fig. 3a). A possible reason may be that STO undergoes no substantial changes of the specific heat at this transition<sup>42</sup>, hence there is no significant influence on the mechanics. It is important to note that optical second-harmonic generation (SHG) measurements, sensitive to structural distortions, performed on this sample still show a prominent feature at around 105 K, as shown in Supplementary Fig. 4 and discussed in Supplementary Note 4.

While the shift in the resonance frequency (Fig. 3a) at 27 K is relatively small, we observe more pronounced features in the mechanical dissipation. To characterize dissipation, we use the quality factor  $Q$  of the resonator (shown in Fig. 3b), which is extracted from the frequency domain measurements as  $Q = f_0/\Delta f$  ( $\Delta f$  is the full width at half maximum of the resonance peak). The overall monotonic decrease of dissipation (increase in  $Q$ ) at lower temperatures is often observed in 2D materials<sup>29,31,43</sup> and in microelectromechanical systems in general<sup>44</sup> and is a subject of ongoing discussion. A proposed explanation for this effect is the increased in-plane tension, which is known to lower dissipation in nanomechanical structures<sup>25,45–47</sup>. Nevertheless, at the temperature of the phase transition we observe an evident change of trend.

Whereas  $f_0$  is influenced by the pre-tension of the membrane and the Young's modulus of the STO, the quality factor is also dependent on the intrinsic losses in the material<sup>46</sup>, which at low temperatures are expected to be dominated by thermoelastic damping. Zener<sup>48</sup> defines a proportionality between the thermoelastic damping term and the specific heat in the following way:  $Q^{-1}(T) \propto \frac{\alpha^2(T)T}{c_v(T)}$ , where  $\alpha$  and  $c_v$  are the thermal expansion

coefficient and the specific heat of the material, respectively. Taking  $\alpha \propto c_v$ <sup>49</sup>, we get a direct relationship between the damping and the specific heat  $Q^{-1}(T) \propto c_v(T)T$ . The inverse of the quality factor for the same resonator is plotted in Fig. 3c, which shows an evident peak in the dissipation at around 30 K. Interestingly, the position and the width of the peak are in accordance to the peak in specific heat of STO measured by Durán et al.<sup>50</sup>. In Supplementary Note 5, we discuss similar trends in  $f_0$  and  $Q$  as a function of temperature that were observed in two other drums from the same STO flake (see Supplementary Figs. 5 and 6). For another STO sample ( $h = 16$  nm), the transition was not observed under intrinsic thermally accumulated strain but did reappear with added strain by means of electrostatic gating (Supplementary Fig. 7), suggesting that strain can play a role in stabilization of the anomaly, similar to the proposed effect of defects<sup>51</sup>.

## Discussion

We demonstrated the fabrication of ultrathin mechanical resonators made of epitaxially grown STO and SRO films. Using laser interferometry, we mechanically characterized the nanodrums and showed that they can be used as nanomechanical devices, much like drums made of van der Waals materials<sup>21,22,25,31,52,53</sup>. We show that phase transitions affect the temperature-dependent dynamics of the resonators and that their mechanical dissipation can shed light on the microscopic loss mechanisms, which are often coupled to electronic and magnetic degrees of freedom. This work connects and presents advances in two fields: (i) the field of complex oxides will benefit from a method for probing the mechanical properties of these strongly correlated electron materials in suspended form; (ii) the field of nanomechanics will now have access to a class of atomically engineerable materials and heterostructures with exotic properties that can be used as functional elements in nanoelectromechanical systems (NEMS). Such nanomechanical resonators can be used in self-transducing mechanical devices, suspended Bragg reflectors, bimorphic actuators, and novel thermomechanical and piezoelectric sensors. Furthermore, by decoupling the high-temperature growth of the materials from the device fabrication flow, the presented complex oxide NEMS resonators can be easily integrated into fully functional complementary metal oxide semiconductor devices that cannot tolerate temperatures  $>400$  °C.

## Methods

**Pulsed laser deposition of epitaxial films.** SAO, STO, and SRO films were grown by pulsed laser deposition on TiO<sub>2</sub>-terminated STO(001) substrates. The pulses

were supplied by a KrF excimer laser and the substrate was mounted using two clamps and heated by an infrared laser. SAO and STO were deposited using a laser fluence of  $1.2 \text{ J/cm}^2$ , a substrate temperature of  $850 \text{ }^\circ\text{C}$ , and an oxygen pressure of  $10^{-6}$  mbar. SRO was deposited at  $600 \text{ }^\circ\text{C}$ , with a fluence of  $1.1 \text{ J/cm}^2$  and an oxygen pressure of  $0.1$  mbar. The growth occurred in layer-by-layer mode for SAO and STO, while SRO was grown in step-flow mode. After the deposition, the heterostructures were annealed for 1 h at  $600 \text{ }^\circ\text{C}$  in  $300$  mbar  $\text{O}_2$  and cooled down in the same atmosphere.

**Release and transfer.** The thin films were released by adhering a PDMS layer to the film surface and immersing the stack in water. Dissolution of a  $50\text{-nm}$  SAO layer was found to take approximately 60 min, without stirring or heating the water. After releasing the substrate, the PDMS layer with the thin film was dried using dry  $\text{N}_2$ . The STO and SRO films were transferred onto pre-patterned  $\text{Si}/285 \text{ nm SiO}_2$  substrates using an all-dry deterministic transfer technique<sup>20</sup>. The crystallinity of the thin films before and after their release was investigated by XRD (see Fig. 1b).

**Mechanical characterization.** The mechanical characterization of the resonators (Figs. 2 and 3) was performed with an active position feedback and variable frequency range to ensure that the laser spot is always centred and focussed on the drum. The resonance peaks are recorded with high accuracy (5000 points per measurement) to rule out any measurement artefacts in the interpretation of the data. In order to eliminate potential artefacts stemming from variations in the adhesion between the membranes and the substrate, the samples are thermally cycled prior to the measurement.

**Second harmonic generation.** The optical SHG measurement was performed in a reflection geometry to further confirm the presence of the structural transition seen in the mechanical experiments. The sample was excited by a  $100\text{-fs}$  laser pulse at a central wavelength of  $800 \text{ nm}$  from a regenerative Ti:Sapphire amplified laser system operating at a  $1\text{-kHz}$  repetition rate. The fluence of the laser radiation used in the experiment was in the order of  $10 \text{ mJ/cm}^2$ . The nonlinear optical response at the central wavelength of  $400 \text{ nm}$  was detected using a photomultiplier tube.

## Data availability

The manuscript has associated data in a data repository. The numerical data shown in figures of the manuscript can be downloaded from the Zenodo online repository at <https://doi.org/10.5281/zenodo.3978636>.

Received: 7 May 2020; Accepted: 27 August 2020;

Published online: 18 September 2020

## References

- Dagotto, E. Complexity in strongly correlated electronic systems. *Science* **309**, 257–262 (2005).
- Reyren, N. et al. Superconducting interfaces between insulating oxides. *Science* **317**, 1196–1199 (2007).
- Farokhipoor, S. et al. Artificial chemical and magnetic structure at the domain walls of an epitaxial oxide. *Nature* **515**, 379–383 (2014).
- Holsteen, A., Kim, I. S. & Lauhon, L. J. Extraordinary dynamic mechanical response of vanadium dioxide nanowires around the insulator to metal phase transition. *Nano Lett.* **14**, 1898–1902 (2014).
- Zubko, P. et al. Negative capacitance in multidomain ferroelectric superlattices. *Nature* **534**, 524–528 (2016).
- Manca, N. et al. Selective high-frequency mechanical actuation driven by the  $\text{VO}_2$  electronic instability. *Adv. Mater.* **29**, 1701618 (2017).
- Rondinelli, J. M., May, S. J. & Freeland, J. W. Control of octahedral connectivity in perovskite oxide heterostructures: An emerging route to multifunctional materials discovery. *MRS Bull.* **37**, 261–270 (2012).
- Bhaskar, U. K. et al. A flexoelectric microelectromechanical system on silicon. *Nat. Nanotechnol.* **11**, 263 (2016).
- Paskiewicz, D. M., Sichel-Tissot, R., Karapetrova, E., Stan, L. & Fong, D. D. Single-crystalline  $\text{SrRuO}_3$  nanomembranes: a platform for flexible oxide electronics. *Nano Lett.* **16**, 534–542 (2015).
- Lu, D. et al. Synthesis of freestanding single-crystal perovskite films and heterostructures by etching of sacrificial water-soluble layers. *Nat. Mater.* **15**, 1255–1260 (2016).
- Ji, D. et al. Freestanding crystalline oxide perovskites down to the monolayer limit. *Nature* **570**, 87 (2019).
- Novoselov, K., Mishchenko, A., Carvalho, A. & Neto, A. C. 2D materials and van der Waals heterostructures. *Science* **353**, aac9439 (2016).
- Atalaya, J., Kinaret, J. M. & Isacsson, A. Nanomechanical mass measurement using nonlinear response of a graphene membrane. *EPL* **91**, 48001 (2010).
- Koenig, S. P., Wang, L., Pellegrino, J. & Bunch, J. S. Selective molecular sieving through porous graphene. *Nat. Nanotechnol.* **7**, 728–732 (2012).
- Smith, A. D. et al. Electromechanical piezoresistive sensing in suspended graphene membranes. *Nano Lett.* **13**, 3237–3242 (2013).
- Dolleman, R. J., Davidovikj, D., Cartamil-Bueno, S. J., van der Zant, H. S. J. & Steeneken, P. G. Graphene squeeze-film pressure sensors. *Nano Lett.* **16**, 568–571 (2016).
- Lee, C., Wei, X., Kysar, J. W. & Hone, J. Measurement of the elastic properties and intrinsic strength of monolayer graphene. *Science* **321**, 385–388 (2008).
- Dolleman, R. J. et al. Optomechanics for thermal characterization of suspended graphene. *Phys. Rev. B* **96**, 165421 (2017).
- Davidovikj, D. et al. Nonlinear dynamic characterization of two-dimensional materials. *Nat. Commun.* **8**, 1253 (2017).
- Castellanos-Gomez, A. et al. Deterministic transfer of two-dimensional materials by all-dry viscoelastic stamping. *2D Mater.* **1**, 011002 (2014).
- Bunch, J. S. et al. Electromechanical resonators from graphene sheets. *Science* **315**, 490–493 (2007).
- Castellanos-Gomez, A. et al. Single-layer  $\text{MoS}_2$  mechanical resonators. *Adv. Mater.* **25**, 6719–6723 (2013).
- Cardona, M. Optical properties and band structure of  $\text{SrTiO}_3$  and  $\text{BaTiO}_3$ . *Phys. Rev.* **140**, A651–A655 (1965).
- Tang, Y., Zhu, Y., Liu, Y., Wang, Y. & Ma, X. Giant linear strain gradient with extremely low elastic energy in a perovskite nanostructure array. *Nat. Commun.* **8**, 1–8 (2017).
- Cartamil-Bueno, S. J. et al. High-quality-factor tantalum oxide nanomechanical resonators by laser oxidation of  $\text{TaSe}_2$ . *Nano Res.* **8**, 2842–2849 (2015).
- Landau, L. D., Pitaevskii, L. P. & Lifshitz, E. M. *Electrodynamics of Continuous Media*. (Butterworth-Heinemann, Oxford, 1984).
- Šiškins, M. et al. Magnetic and electronic phase transitions probed by nanomechanical resonators. *Nat. Commun.* **11**, 1–7 (2020).
- Sanditov, D. & Belomestnykh, V. Relation between the parameters of the elasticity theory and averaged bulk modulus of solids. *Tech. Phys. Lett.* **56**, 1619–1623 (2011).
- Chen, C. et al. Performance of monolayer graphene nanomechanical resonators with electrical readout. *Nat. Nanotechnol.* **4**, 861–867 (2009).
- Singh, V. et al. Probing thermal expansion of graphene and modal dispersion at low-temperature using graphene nanoelectromechanical systems resonators. *Nanotechnology* **21**, 165204 (2010).
- Morell, N. et al. High quality factor mechanical resonators based on  $\text{WSe}_2$  monolayers. *Nano Lett.* **16**, 5102–5108 (2016).
- Scott, J. & Ledbetter, H. Interpretation of elastic anomalies in  $\text{SrTiO}_3$  at  $37 \text{ K}$ . *Z. Phys. B Condens. Matter* **104**, 635–639 (1997).
- Kityk, A. et al. Nonlinear elastic behaviour of  $\text{SrTiO}_3$  crystals in the quantum paraelectric regime. *EPL* **50**, 41 (2000).
- Zalar, B. et al. NMR study of disorder in  $\text{BaTiO}_3$  and  $\text{SrTiO}_3$ . *Phys. Rev. B* **71**, 064107 (2005).
- Scott, J. F., Salje, E. K. H. & Carpenter, M. A. Domain wall damping and elastic softening in  $\text{SrTiO}_3$ : evidence for polar twin walls. *Phys. Rev. Lett.* **109**, 187601 (2012).
- Salje, E. K. H., Aktas, O., Carpenter, M. A., Laguta, V. V. & Scott, J. F. Domains within domains and walls within walls: evidence for polar domains in cryogenic  $\text{SrTiO}_3$ . *Phys. Rev. Lett.* **111**, 247603 (2013).
- Ledbetter, H., Lei, M. & Kim, S. Elastic constants, Debye temperatures, and electron-phonon parameters of superconducting cuprates and related oxides. *Phase Transit.* **23**, 61–70 (1990).
- Ang, C., Scott, J. F., Yu, Z., Ledbetter, H. & Baptista, J. L. Dielectric and ultrasonic anomalies at  $16$ ,  $37$ , and  $65 \text{ K}$  in  $\text{SrTiO}_3$ . *Phys. Rev. B* **59**, 6661–6664 (1999).
- Tsunekawa, S., Watanabe, H. & Takei, H. Linear thermal expansion of  $\text{SrTiO}_3$ . *Phys. Status Solidi A* **83**, 467–472 (1984).
- Lytle, F. W. X-ray diffractometry of low-temperature phase transformations in strontium titanate. *J. Appl. Phys.* **35**, 2212–2215 (1964).
- Unoki, H. & Sakudo, T. Electron spin resonance of  $\text{Fe}^{3+}$  in  $\text{SrTiO}_3$  with special reference to the  $110 \text{ K}$  phase transition. *J. Phys. Soc.* **23**, 546–552 (1967).
- Garnier, P. Specific heat of  $\text{SrTiO}_3$  near the structural transition. *Phys. Lett. A* **35**, 413–414 (1971).
- Will, M. et al. High quality factor graphene-based two-dimensional heterostructure mechanical resonator. *Nano Lett.* **17**, 5950–5955 (2017).
- Kim, B. et al. Temperature dependence of quality factor in MEMS resonators. *J. Microelectromech. Syst.* **17**, 755–766 (2008).
- Verbridge, S. S., Parpia, J. M., Reichenbach, R. B., Bellan, L. M. & Craighead, H. High quality factor resonance at room temperature with nanostrings under high tensile stress. *J. Appl. Phys.* **99**, 124304 (2006).
- Unterreithmeier, Q. P., Faust, T. & Kotthaus, J. P. Damping of nanomechanical resonators. *Phys. Rev. Lett.* **105**, 027205 (2010).

47. Norte, R. A., Moura, J. P. & Gröblacher, S. Mechanical resonators for quantum optomechanics experiments at room temperature. *Phys. Rev. Lett.* **116**, 147202 (2016).
48. Zener, C. Internal friction in solids. I. Theory of internal friction in reeds. *Phys. Rev.* **52**, 230 (1937).
49. Garai, J. Correlation between thermal expansion and heat capacity. *Calphad* **30**, 354–356 (2006).
50. Durán, A., Morales, F., Fuentes, L. & Siqueiros, J. Specific heat anomalies at 37, 105 and 455 K in SrTiO<sub>3</sub>:Pr. *J. Condens. Matter Phys.* **20**, 085219 (2008).
51. Arzel, L. et al. Observation of a sample-dependent 37 K anomaly on the lattice parameters of strontium titanate. *EPL* **61**, 653 (2003).
52. Wang, Z. et al. Black phosphorus nanoelectromechanical resonators vibrating at very high frequencies. *Nanoscale* **7**, 877–884 (2015).
53. Cartamil-Bueno, S. J. et al. Mechanical characterization and cleaning of CVD single-layer h-BN resonators. *npj 2D Mater. Appl.* **1**, 16 (2017).

### Acknowledgements

The authors thank Pavlo Zubko and Gustau Catalan for the fruitful discussions and extensive feedback. This work was supported by the Dutch Research Council (NWO/OCW), as part of the Frontiers of Nanoscience (NanoFront) program, by the Dutch Foundation for Fundamental Research on Matter (FOM), by the European Research Council under the European Union's H2020 programme/ERC Grant Agreement No. [677458], by the European Union Seventh Framework Programme under grant agreement no. 604391 Graphene Flagship, and by the European Union's Horizon 2020 research and innovation programme under grant agreement nos. 785219 and 881603.

### Author contributions

D.J.G., A.M.V.R.L.M., and A.D. deposited and characterized the epitaxial heterostructures and prepared the suspended films. D.D. and D.J.G. performed the measurements and analysed the data. M.Š. and M.L. performed the measurements on the additional samples. D.D., D.J.G., A.M.V.R.L.M., M.Š., M.L., H.S.J.v.d.Z., A.D.C., and P.G.S. interpreted the data. D.A. performed the second-harmonic generation measurements. Y.H. and E.v.H.

synthesized the SAO target for pulsed laser deposition. P.G.S. and A.D.C. supervised the overall project. D.D., D.J.G., A.D.C., and P.G.S. wrote the manuscript with input from all authors.

### Competing interests

The authors declare no competing interests.

### Additional information

Supplementary information is available for this paper at <https://doi.org/10.1038/s42005-020-00433-y>.

Correspondence and requests for materials should be addressed to A.D.C. or P.G.S.

Reprints and permission information is available at <http://www.nature.com/reprints>

Publisher's note Springer Nature remains neutral with regard to jurisdictional claims in published maps and institutional affiliations.



**Open Access** This article is licensed under a Creative Commons Attribution 4.0 International License, which permits use, sharing, adaptation, distribution and reproduction in any medium or format, as long as you give appropriate credit to the original author(s) and the source, provide a link to the Creative Commons license, and indicate if changes were made. The images or other third party material in this article are included in the article's Creative Commons license, unless indicated otherwise in a credit line to the material. If material is not included in the article's Creative Commons license and your intended use is not permitted by statutory regulation or exceeds the permitted use, you will need to obtain permission directly from the copyright holder. To view a copy of this license, visit <http://creativecommons.org/licenses/by/4.0/>.

© The Author(s) 2020